

Deep learning-based optical approach for skin analysis of melanin and hemoglobin distribution

Geunho Jung¹,* Semin Kim¹, Jongha Lee¹, and Sangwook Yoo

Lulu-lab, AI R&D Center, Seoul, Republic of Korea

Abstract

Significance: Melanin and hemoglobin have been measured as important diagnostic indicators of facial skin conditions for aesthetic and diagnostic purposes. Commercial clinical equipment provides reliable analysis results, but it has several drawbacks: exclusive to the acquisition system, expensive, and computationally intensive.

Aim: We propose an approach to alleviate those drawbacks using a deep learning model trained to solve the forward problem of light–tissue interactions. The model is structurally extensible for various light sources and cameras and maintains the input image resolution for medical applications.

Approach: A facial image is divided into multiple patches and decomposed into melanin, hemoglobin, shading, and specular maps. The outputs are reconstructed into a facial image by solving the forward problem over skin areas. As learning progresses, the difference between the reconstructed image and input image is reduced, resulting in the melanin and hemoglobin maps becoming closer to their distribution of the input image.

Results: The proposed approach was evaluated on 30 subjects using the professional clinical system, VISIA VAESTRO. The correlation coefficients for melanin and hemoglobin were found to be 0.932 and 0.857, respectively. Additionally, this approach was applied to simulated images with varying amounts of melanin and hemoglobin.

Conclusion: The proposed approach showed high correlation with the clinical system for analyzing melanin and hemoglobin distribution, indicating its potential for accurate diagnosis. Further calibration studies using clinical equipment can enhance its diagnostic ability. The structurally extensible model makes it a promising tool for various image acquisition conditions.

© The Authors. Published by SPIE under a Creative Commons Attribution 4.0 International License. Distribution or reproduction of this work in whole or in part requires full attribution of the original publication, including its DOI. [DOI: [10.1117/1.JBO.28.3.035001](https://doi.org/10.1117/1.JBO.28.3.035001)]

Keywords: skin analysis; deep learning; light–tissue interaction; melanin; hemoglobin; VISIA.

Paper 220286GR received Dec. 1, 2022; accepted for publication Mar. 6, 2023; published online Mar. 27, 2023.

1 Introduction

The optical properties of human skin have been studied for various purposes. Skin layers are optically modeled in computer vision for a detailed description of the face.^{1,2} In dermatology, light absorption and scattering are the main principles for diagnosing skin conditions.^{3,4} In biomedical research, the distribution of chromophores and hemodynamic changes are imaged using diffuse optical tomography,⁵ optical coherence tomography,⁶ and spatial frequency domain imaging.⁷

In terms of skin analysis equipment, the optical measurement approach has various advantages compared to other imaging modalities: non-invasive, relatively safe, and real-time or frequent measurements. As examples of single-measurement devices, the Mexameter, Sebumeter, and Visiometer can be used to quantify pigmentation, oiliness, and wrinkles, respectively.^{8,9} Multifunctional systems utilize image processing techniques to skin images acquired from

*Address all correspondence to Geunho Jung, gh.jung@lulu-lab.com

well-constructed optical systems with minimal ambient light. For example, VISIA, Robo skin analyzer, and DermaVision provide the ability to measure melanin, hemoglobin, wrinkles, and pores.¹⁰⁻¹²

Multifunctional systems analyze shape and color-related skin information based on the optical properties of human skin. The shape features, such as the skin surface and facial structure, are enhanced in the specular light images, and the wrinkles^{13,14} and pores¹⁵ belong to these features. Skin color is the result of the interactions between light and skin chromophores such as melanin and hemoglobin,¹⁶ and this feature is enhanced in cross-polarized images.¹⁷ For accurate measurements, clinical multi-functional systems are used to acquire and analyze skin images with ambient light blocked. Despite the fact that these professional systems have produced reliable analysis results and are widely used in clinics, they have several limitations: the analytical tool is dedicated to the image acquisition system. Images should be acquired in a specific environment and this result in a lack of versatility. The image acquisition system and analysis tools require a high cost, and the analysis process is time-consuming due to the complex calculations involved, such as fitting for each pixel. This is particularly important in medical applications that require high-resolution images, even if it needs high computational resources and time.

To alleviate those limitations, we propose a novel approach using a deep learning model trained to solve the forward problem of light–tissue interactions. The model is structurally extensible for various light sources and cameras and it maintains the resolution of the input image for medical applications. The proposed approach is evaluated with the professional clinical system, VISIA VAESTRO. In addition, this approach was applied to simulations with varying amounts of melanin and hemoglobin.

2 Methods

The concept of the decomposition structure is based on the reference study in Ref. 18. The referenced structure has been modified and extended to include a skin segmentation model, patch divider and combiner, and virtual ColorChecker in Fig. 1 and verified for medical applications.

2.1 Skin Segmentation Model

As the forward model is based on the optical properties of the skin, it is necessary to separate non-skin areas, such as the background, eyes, nostrils, and lips. To extract the skin area from any face image, we developed a skin segmentation model using a lightened structure of the basic

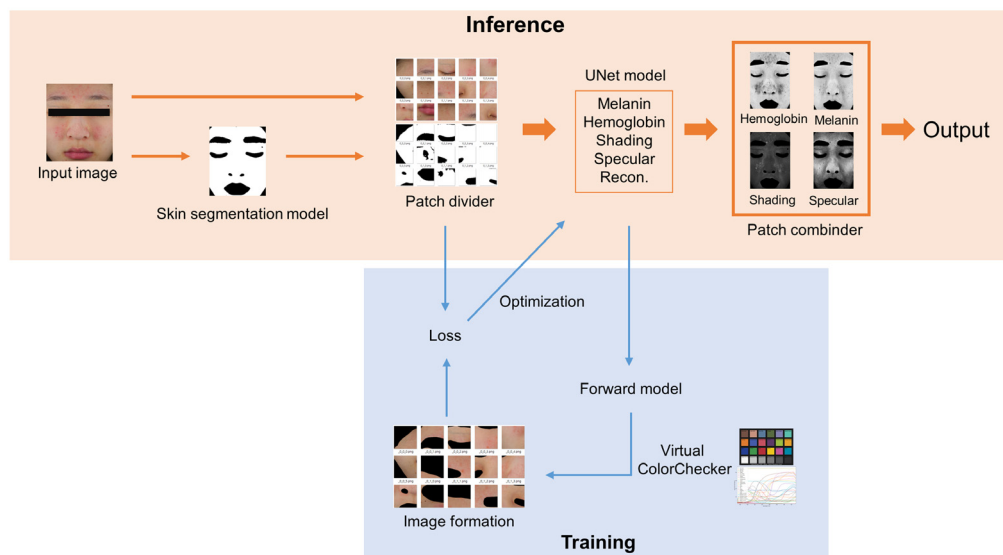


Fig. 1 Diagram of the entire system: the training and inference processes.

U-Net model with reduced number of channels. The model was trained using 380 images with an input and output size of 640×480 pixels, achieving a performance of CIoU 0.95.

2.2 Patch Divider and Combiner

When a high-resolution image is resized to the UNet input size, the detailed features of the image are lost. This loss could be a critical problem in medical applications where diagnostics require detailed characteristics. Therefore, the input image is divided into multiple patches to maintain the input image resolution. To remove borderlines that may appear after merging, the patches are combined by multiplying the overlapping areas by the gradient weight, and the overlapping area is added to the patch size. Since the image acquisition conditions for all patches are the same, the skin’s optical properties do not change even if analyzed in units of patches. In this study, the input image is divided into 4×6 patches with a size of 256×256 pixels for inference.

After dividing into patches, the gamma correction is inverted by Eq. 1 to make the image linear,

$$I_{\text{rgb}} = \left(\frac{I_{\text{srgb}} + 0.055}{1.055} \right)^{2.4}, \tag{1}$$

where I_{srgb} is the input color image in the sRGB color space, while I_{rgb} is the corresponding image in the RGB color space with inverted gamma correction.

2.3 UNet Model and Training Conditions

Figure 2 shows the architecture of the UNet model used for image decomposition. For training, the model is initialized with the pretrained model for the Carvana dataset. The Adam optimizer is used with l2 weight decay and a cosine annealing scheduler. The mean squared error (MSE) is employed as a loss function, and the peak signal-to-noise ratio (PSNR) is used to estimate the similarity between reconstructed and original skin images. The python library “albumentation” is used to augment the training dataset by randomly flipping, scaling, and rotating it.

The proposed model decomposes a color image into four outputs: melanin, hemoglobin, shading, and specular maps, allowing for the separation of the face image into its color and morphological components. Shading is used to add depth to a flat image and create a three-dimensional appearance. Specular represents light that is directly reflected from the skin surface and includes morphological elements constituting the input image, such as surface shape and roughness, as well. This study primarily focuses on color-related skin components, melanin and

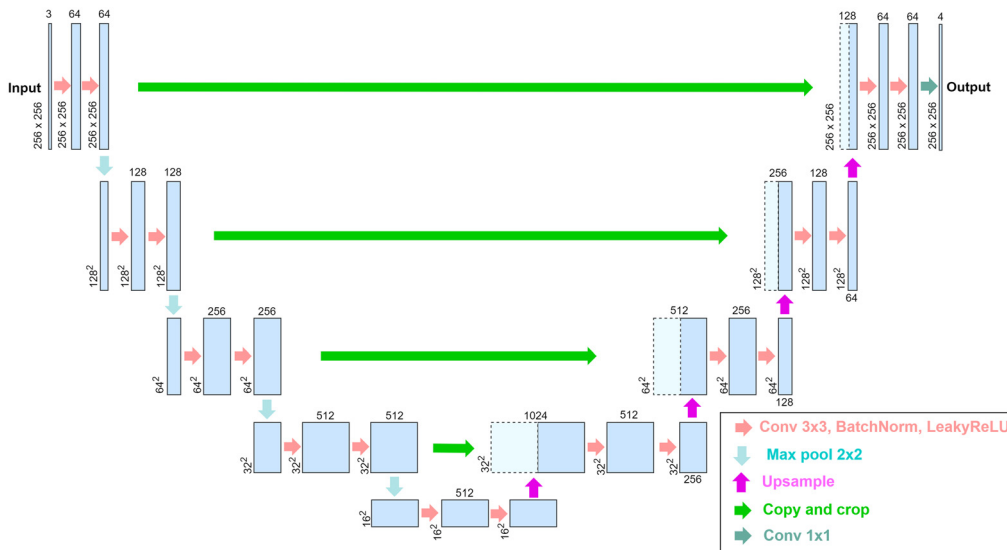


Fig. 2 Architecture for the image decomposition: the UNet model.

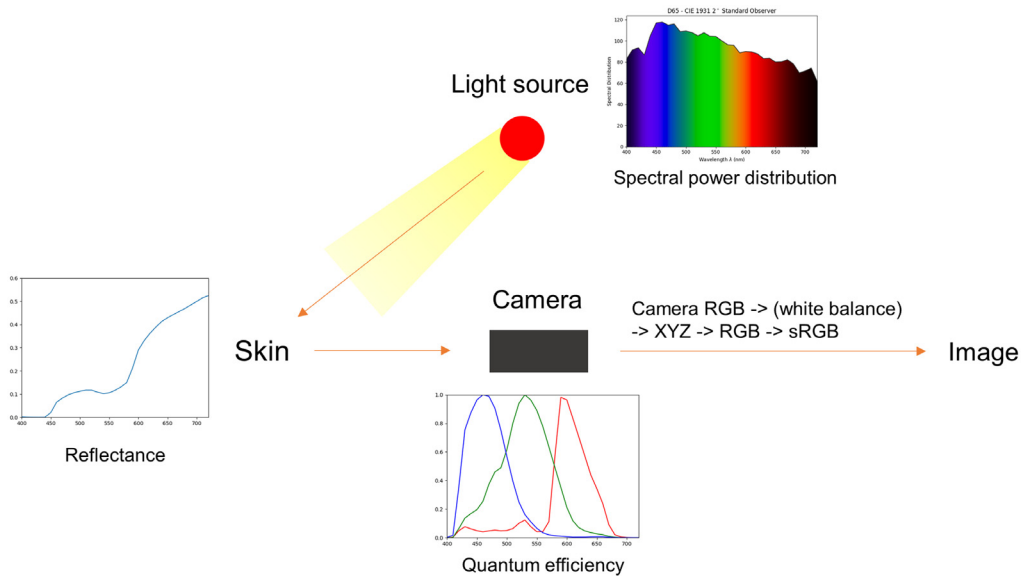


Fig. 3 Schematic diagram of the skin image acquisition process.

hemoglobin maps. As skin color is also affected by morphological factors, shading and specular maps are incorporated into the structure to account for their effects.

2.4 Forward Model

2.4.1 Image acquisition. Figure 3 shows a schematic diagram of the skin image acquisition process, in which light emitted from the source is reflected from the skin, detected by a camera, and formed into an image. The spectral characteristics of a light source, which cover all light that affects the image including ambient light, are expressed using spectral power distribution (SPD). In a typical measurement environment, the light source is a combination of various indoor lights and sunlight. In controlled conditions where ambient light is blocked, and images are acquired using professional equipment, the SPD of the light source of the equipment is supplied by the manufacturer's specifications. In uncontrolled conditions, where images are acquired in an open environment, images are affected by various light sources, and the SPD can be measured directly using a spectrometer. Most of the light that illuminated the skin is diffused into the skin layers, and the rest is reflected from the surface. In the skin layers, visible light is mainly absorbed by melanin and hemoglobin and scattered exponentially as a function of wavelength.^{19,20} Skin reflectance is affected by various factors, including the scattering properties of the skin as well as the absorption of the melanin and hemoglobin, which have been extensively researched.^{21–24} The specular light and diffusely reflected light are detected as photons by the camera sensor and then converted into electrical signals according to the quantum efficiency of the camera to form an image. This image is in a RGB color space dependent on the camera device and is sequentially converted to the common color space XYZ, RGB, and sRGB.²⁵

2.4.2 Forward and inverse problem. Under a given light and skin reflectance, the diffusely reflected light is predicted as a unique solution to a forward problem. The radiative transfer equation (RTE), diffuse equation,²⁶ or a stochastic methods Monte Carlo simulation^{27,28} can be used to solve this mathematical model. Acquiring skin images and analyzing skin components is the opposite process. It is difficult to obtain the actual values of skin properties because skin is a scattering-dominant material. Therefore, it has been predicted by solving the inverse problem using Inverse Monte Carlo,^{29,30} principal component analysis (PCA),³¹ independent component analysis (ICA),³² or polynomial fitting.³³ During the fitting process, different skin property values are iteratively given, and the corresponding forward problems are solved until the error becomes lower than the threshold. It requires enough time to repeatedly calculate the forward problem for each pixel of the whole image. As the forward problem has been studied for a long

time and applied to various studies,^{34,35} it is considered reliable and used to train the proposed model.

2.4.3 Acquisition conditions. The image acquisition environment must be set in advance to proceed with the forward model. There are two factors: a light source and camera sensitivity. In this study, skin images were acquired using the “VISIA-CR” system. To ensure consistency between image acquisition and analysis conditions, the spectral data of the standard illuminant “D65” in ISO 2002 and the camera sensitivity of the “Canon 5D Mark II”^{36,37} within the wavelength range of 400 to 720 nm are used. The spectrum of the light source is normalized by inversely multiplying a scaling factor, which is derived by multiplying the light source and the maximum sensitivity value of the camera channels.

2.4.4 Optical modeling of skin layers. The epidermis is the outermost layer of the skin. In the epidermis layer, light is absorbed by melanin and scattered by keratin fibers. However, the change in light direction could be ignored because of the thin thickness. In the dermis layer, light mainly experiences absorption in the hemoglobin of the capillaries and blood vessels, and scattering in collagen fibers and elastin fibers.³⁸ Therefore, skin layers are optically modeled as follows: the epidermis is modeled as a melanin absorption layer, and the dermis is modeled as a combination of a hemoglobin absorption layer and multiple scattering layers. The measured light includes both the specular reflected light from the skin surface and the diffusely reflected light that is absorbed in the epidermis and dermis layers.

2.4.5 Skin reflectance. The Kubelka–Munk theory is one of the popular methods for modeling light reflection in skin layers.^{39,40} Assuming that light is reflected only from the dermis layer, the simplified form of the theory is represented as follows:

$$R(\lambda) = T_{\text{epidermis}}(\lambda)^2 R_{\text{dermis}}(\lambda), \quad (2)$$

where $T_{\text{epidermis}}$ represents the fraction of light that transmitted the epidermis, and R_{dermis} refers to the fraction of light reflected from the dermis layer.

The absorption and reduced scattering coefficient are shown in Eqs. (3) and (4).⁴¹ In a method which precisely measures in a wider wavelength range, such as diffuse reflectance spectroscopy, more chromophores can be included in Eq. (3), such as met-hemoglobin, water, lipid, and beta-carotene^{42,43}

$$\mu_a(\lambda) = \sum_i S_i \epsilon_i(\lambda) C_i, \quad (3)$$

$$\mu'_s(\lambda) = a \left(f_{\text{Ray}} \left(\frac{\lambda}{\lambda_0} \right)^{-4} + (1 - f_{\text{Ray}}) \left(\frac{\lambda}{\lambda_0} \right)^{-b_{\text{Mie}}} \right), \quad (4)$$

where S_i is the volume fraction, ϵ_i is the extinction coefficient, C_i is the concentration for i in melanin and hemoglobin, a is the scattering amplitude, b_{Mie} is the scattering power of Mie scattering, and f_{Ray} is the fraction of scattering events as Rayleigh scattering.

The reflectance can be obtained through the diffusion equation.⁴² In this study, the skin reflectance calculated from Refs. 18, 34, and 44 is used based on the Kubelka-Munk theory. The volume fraction of the melanin is limited to a range of 1.3% to 43%, and the hemoglobin is in the range of 2% to 7%.^{45–47}

2.4.6 Image formation. The camera image measured by the sensor is described for each color channel m

$$I_m = \int_{\lambda_{\min}}^{\lambda_{\max}} L(\lambda) R(\lambda) C_m(\lambda) d\lambda, \quad (5)$$

where $L(\lambda)$ is the SPD of the light source, $R(\lambda)$ is the skin reflectance, $C_m(\lambda)$ is the camera sensitivity of color channel $m \in \{r, g, b\}$. In this study, $\lambda_{\min} = 450$ nm and $\lambda_{\max} = 750$ nm.

The light entering the camera is affected by the light source and skin reflectance $[L(\lambda)R(\lambda)]$ in Eq. (5) and consists of specular and diffusely reflected light

$$I_m = \int_{\lambda_{\min}}^{\lambda_{\max}} (I_{d(m)}(\lambda) + I_{s(m)}(\lambda))C_m d\lambda, \quad (6)$$

$$I_{d(m)}(\lambda) = L(\lambda)R(\lambda)M_{\text{shading}}(\lambda), \quad (7)$$

$$I_{s(m)}(\lambda) = L(\lambda)M_{\text{specular}}(\lambda), \quad (8)$$

where M_{shading} and M_{specular} are the model outputs, the shading and specular maps; $I_{d(m)}(\lambda)$ and $I_{s(m)}(\lambda)$ are the diffuse and specular images for each color channel m ; and $I_{\text{cam}} = [I_r, I_g, I_b]$ is the camera image. The diffusely reflected light is influenced by the geometry of the face and the skin reflectance through optical interaction with the skin components in Eq. (7), whereas the specular light is directly reflected from the skin surface and is significantly affected by the geometry of the face in Eq. (8).

2.4.7 Color transformation matrix with virtual ColorChecker. A transformation matrix is required to convert between different color spaces. Considering its applicability in various acquisition systems and environments, the reflectance of the 24-patch version of ColorChecker⁴⁸ is employed in Fig. 4. Given a light source and ColorChecker, it is possible to theoretically compute the RGB value of the camera and the XYZ (CIE 1931 2 degree standard observer) value for each color patch. The transformation matrix between different color spaces is derived by polynomial expansion.⁴⁹ In this study, this method is specified as the ‘‘Virtual ColorChecker’’ and implemented using the Python Colour-Science library.

2.4.8 Image formation. White balance is a normalization process that divides the sensor’s intensity by the value when the light source is directly detected I_m

$$\begin{bmatrix} I_{wb(r)} \\ I_{wb(g)} \\ I_{wb(b)} \end{bmatrix} = \begin{bmatrix} 1/I_r & 0 & 0 \\ 0 & 1/I_g & 0 \\ 0 & 0 & 1/I_b \end{bmatrix} \begin{bmatrix} I_r \\ I_g \\ I_b \end{bmatrix}. \quad (9)$$

The color space of the camera image is an inherent characteristic of a camera device. It should be converted to the common color spaces XYZ, RGB, and sRGB, sequentially. The color space is converted by multiplying the color transformation matrix, and the sRGB image is obtained by applying gamma correction to RGB in Eq. (10). In this study, it is assumed that a minimally processed image captured by the camera is used

$$I_{\text{srgb}} = 1.055I_{\text{rgb}}^{(1/2.4)} - 0.055, \quad (10)$$

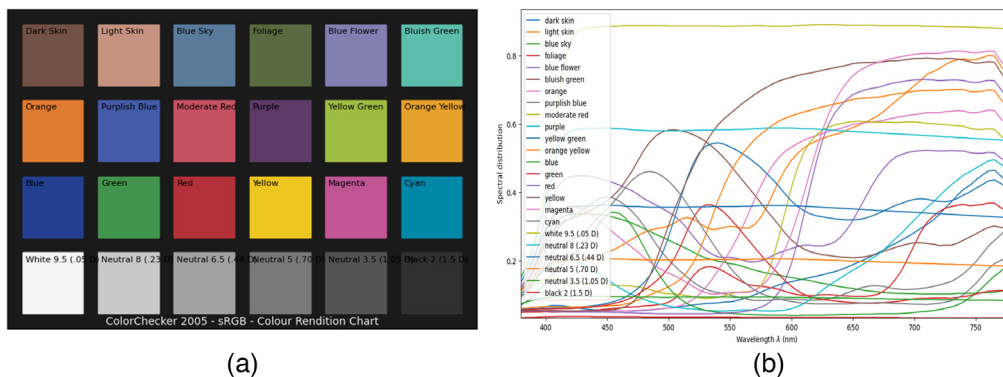


Fig. 4 (a) Plate of the ColorChecker 2005 and (b) its reflectance measurements in Ref. 48.

where I_{rgb} is an image in the RGB color space, and I_{srgb} is the gamma corrected image in the sRGB color space.

2.5 Metrics

To quantify the performance of the proposed model, three methods are employed in this study: the MSE, PSNR, and the Pearson product-moment correlation coefficients.^{50,51} For training and validation, the MSE and PSNR are used to estimate the similarity between the input and reconstructed images, indirectly improving the melanin and hemoglobin analysis ability. After training, the correlation coefficient is used to directly compare the results with the clinical equipment, VISIA system. Since the VISIA system produces single-color distribution maps with red and brown for hemoglobin and melanin, respectively, they are converted to grayscale and employed for comparison.

2.6 Experiments

The polarized image dataset was acquired from 198 subjects using the VISIA acquisition system, VISIA-CR. The dataset was divided into 2 groups: 168 subjects for model training and 30 subjects for testing the performance of the trained model. Facial images were collected with informed consent from all subjects, in accordance with all relevant national regulations and institutional policies, and approved by the authors' institutional committees. The training images are divided into 20 patches (4×5) of 310×310 pixels and randomly cropped to 256×256 pixels during augmentation for reducing overfitting and improving robustness of the model. For testing, the images are divided into 24 patches (4×6) of 256×256 pixels. These patches are used as inputs to the model, and the output patches are combined to form a full image. To avoid the occurrence of blurry lines on the border of output patches, boundary areas are overlapped by 15 pixels and combined by multiplying the opposite gradient weights. Including the overlapping boundary areas, the combined output size is 979×1461 pixels. Finally, the proposed model and VISIA VAESTRO system are compared to analyze the correlation of the two system measurements for melanin and hemoglobin. The VISIA VAESTRO system is the integrated skin analysis toolkits including the melanin and hemoglobin analysis modules, RBX-Brown and RBX-Red Processing 1.0.^{52,53} To avoid repetition of software name throughout this manuscript, we will use the term VISIA system to refer to this analysis system. In addition, this approach is applied to simulated images with varying amounts of melanin and hemoglobin.

3 Results

The proposed model decomposes the skin segmented area into hemoglobin, melanin, shading, and specular components that are combined to reconstruct the skin image, as shown in Fig. 5. The trained model achieved an average PSNR value of 42.7, and an example of the input and reconstructed images is shown in Fig. 5. The analyzed results of the hemoglobin and melanin obtained from the proposed model and the VISIA system are shown in Fig. 6 and their correlation coefficients according to training epochs are shown in Fig. 7. As the hemoglobin and melanin values increase, the intensity in grayscale image decreases in the VISIA system, while it increases in the proposed method. To facilitate comparison between the two methods, the grayscale images produced by the proposed method are inverted in Figs. 5 and 6. The results of the proposed model for seven different epochs are postprocessed and compared to the VISIA system. The correlation coefficient is 0.932 (std 0.083) for melanin and 0.857 (std 0.155) for hemoglobin in 2900 epochs.

The simulated images by manipulating its melanin and hemoglobin levels in the skin are shown in Fig. 8. The simulated images are generated by modifying the center image with changes to melanin (multiplying by -1.2 and $+1.2$) and hemoglobin (adding -1 and $+1$) levels.

4 Discussion

The average PSNR value of the trained model exceeds 30, which indicates a high degree of similarity⁵⁴ between the input and reconstructed images, shown in Fig. 5. The proposed model

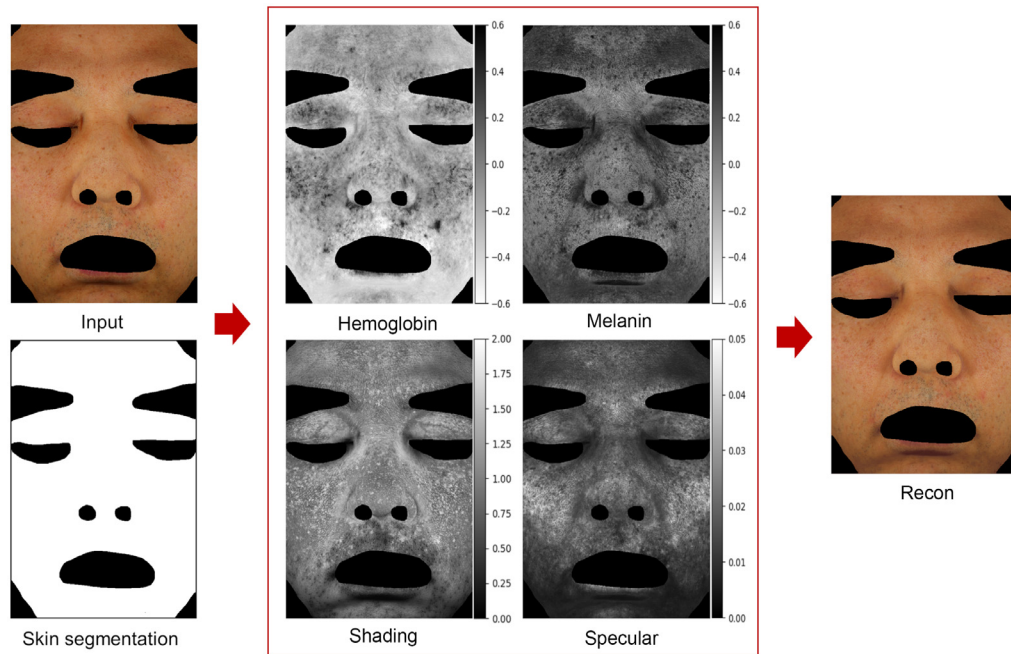


Fig. 5 Decomposed (inverted in hemoglobin and melanin) and reconstructed images produced by the proposed model.

and the VISIA system show a similar tendency in Fig. 6, especially the melanin map has a higher overall value in (upper) dark skin than in (lower) lighter skin. The exact value of human skin properties is difficult to determine. Therefore, the proposed approach's performance is evaluated by comparing it with one of the most reliable clinical equipment systems, the VISIA system.^{11,52,55} This implies that the correlation values are a comparison to determine the strength and direction of the relationship between the two systems, rather than an absolute accuracy of skin measurements. The proposed model is considered sufficiently trained at around 200 epochs, with correlation coefficients of 0.932 and 0.857 for melanin and hemoglobin, as shown in Fig. 7. Considering that image processing and deep learning are different approaches and the results of

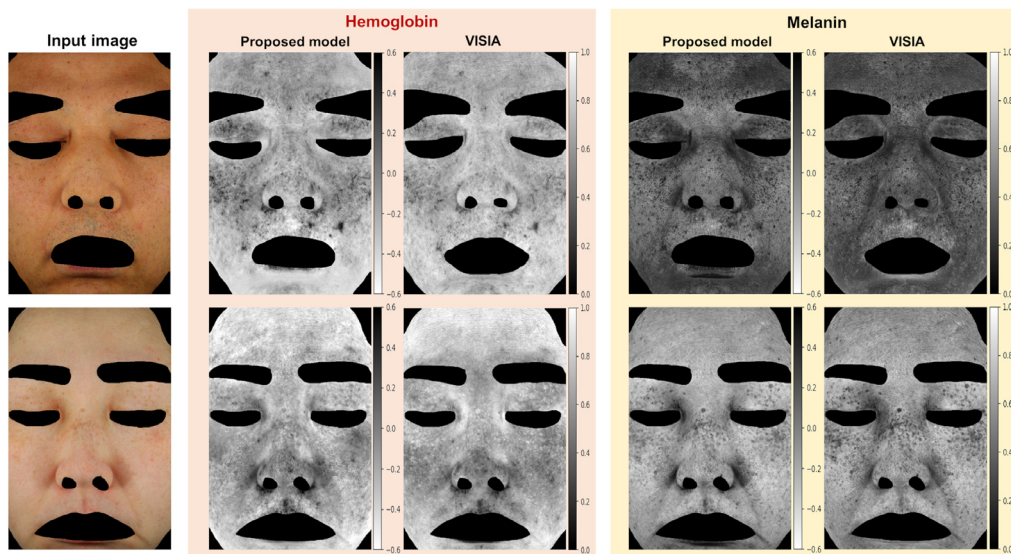


Fig. 6 Hemoglobin and melanin analysis results from the proposed model (inverted) and VISIA system.

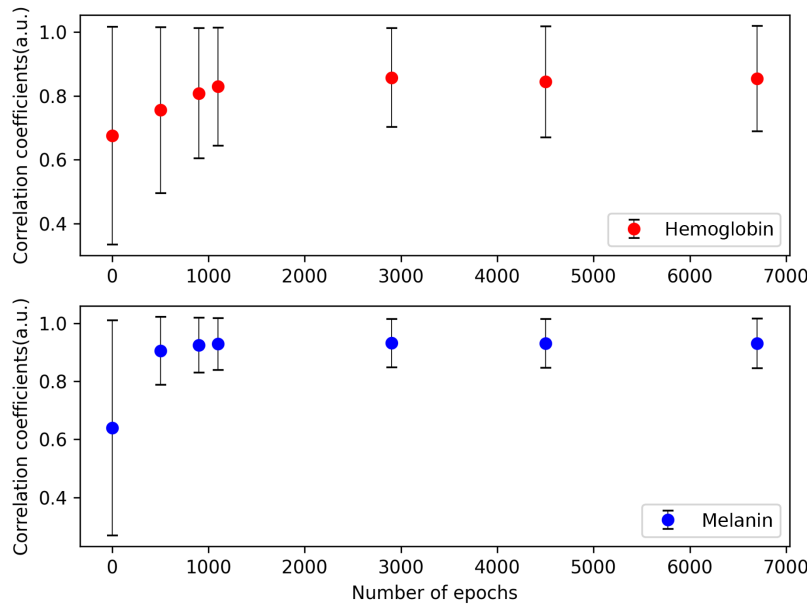


Fig. 7 Correlation coefficients between the proposed model and the VISIA system depending on the number of epochs in training.

the VISIA system are not used in training, this strong positive relationship with clinical equipment can be interpreted as the light–tissue interactions being learned well as intended.

However, the VISIA system outperforms our proposed model, especially in terms of capturing detailed features. As an example, Fig. 9 shows the right corner of the mouth area from the melanin maps of the upper line in Fig. 6. When considering the input image, it is reasonable that the red spot in the result of the proposed method should not be emphasized like in the VISIA system. When the correlation coefficient is calculated by excluding the red spot, the difference in the coefficient is only 0.002. This insignificant value indicates that small differences in detailed areas are challenging to capture using overall representative values.

Besides the results, there are factors that can potentially affect the correlation values. The overall pixel values in the image can change depending on the plotting range when converting the analysis results into an image. This issue applied to both the proposed model and the VISIA system. To mitigate it, we conducted the analysis with constant plotting options for both systems. The VISIA system used the optimal conditions determined through postprocessing as a constant in the analysis process. To compare the analysis results of both systems, we calculated the correlation coefficients of the entire image rather than comparing the pixel intensity alone. This approach minimizes the effects caused by this issue. Next, the format of the result image differs between the single-color distribution map of the VISIA system and the grayscale image of the proposed model. It is possible that a slight difference may occur in the process of converting the color image to grayscale for the VISIA system.

The proposed approach has demonstrated the potential for generating simulated images with varying amounts of melanin and hemoglobin, as shown in Fig. 8. While changes in melanin and hemoglobin levels do affect skin tone, it is important to note that further research and verification are needed to accurately represent these changes in simulated images.

For diagnostic purposes, the following studies could be conducted. The forward model applied in the training part aims to find the absolute amount of skin components. If the range of output values and plotting options are calibrated with clinical equipment that supplies absolute values, such as Mexameter, the proposed model could be used for evaluating the severity of the disease. Furthermore, this study primarily focuses on color-related information, while the morphological characteristics are mainly utilized for accounting for color changes caused by shape-related features. If a follow-up study is conducted to enhance the morphological features of the specular map by modifying the learning process or applying postprocessing, the proposed method could be extended to the diagnosis of wrinkles and pores. Finally, the proposed model

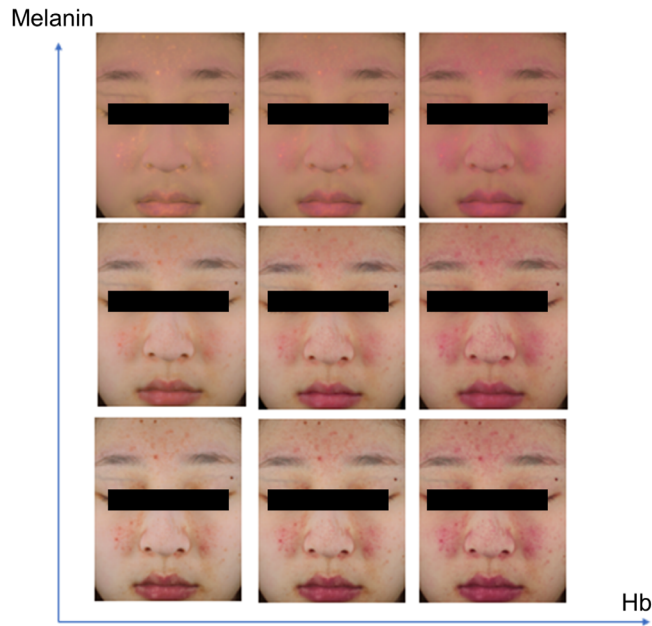


Fig. 8 Simulated images for melanin and hemoglobin.

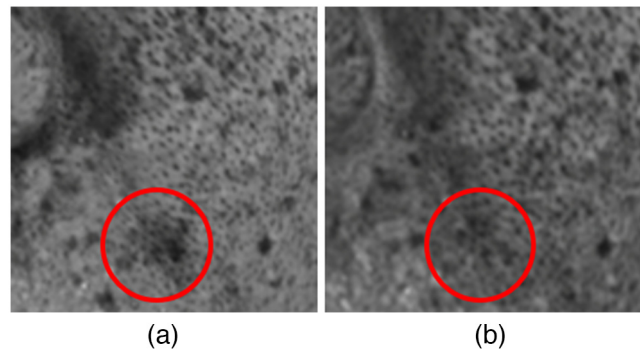


Fig. 9 Magnified area of the melanin map from (a) the proposed model and (b) the VISIA system.

requires prior knowledge of the light source and camera information. If an additional algorithm is applied to estimate that spectrum information, the range of application will be expanded to images acquired from uncontrolled environments.

To enhance the performance of the proposed model, the following methods are considered. First, using the results of the VISIA system as ground truth (GT) during training can potentially improve the model's performance by providing detailed information about skin properties. However, in this study, we intentionally chose not to use any GT for skin images to focus on investigating the performance of the proposed model in implementing light interaction with the skin. Using GTs is a standard practice for training deep learning models, and modifying the proposed model to include GTs will require extensive trials to optimize performance while preserving the advantages of both the current method and GTs. Second, in this study, a lightweight version of the basic U-Net model is employed to ensure efficient computational time. However, if the model prioritizes high performance over shorter analysis time and memory capacity, it may be worth trying model structures that use more parameters and take longer computational time but have superior performance. Finally, training with a large number of datasets and measuring accurate SPD using a spectrometer can help improve accuracy.

5 Conclusion

In this study, we trained a deep learning model to solve the forward problem of light–tissue interactions and its performance was evaluated using professional clinical equipment, the VISIA system. The model is structurally extensible for various acquisition conditions, and the skin segmentation model, patch divider and combiner, and virtual ColorChecker methods are applied for medical applications. The results showed a high correlation coefficients for melanin and hemoglobin. In addition, this approach was applied to simulated images with varying amounts of melanin and hemoglobin. It is expected that the proposed approach will be further developed for skin analysis and disease diagnosis through calibration studies using clinical equipment, ultimately providing a valuable tool for dermatologists and clinicians.

Disclosures

The authors have no relevant financial interests in this article and no potential conflicts of interest to disclose.

Acknowledgments

This research was supported by Technological Innovation Project (Grant No. S3197480) from the “Ministry of SMEs and Startups” and NIPA. The research data were supplied by GMRC (Global Medical Research Center, Republic of Korea).

Code, Data and Materials Statement

The code associated with this article is available upon request sent to the corresponding author. The image dataset is subject to institutional restrictions and can only be used for research purposes with the prior consent of the subjects and the approval of the author’s institutional committees. These restrictions are in place to protect the privacy and confidentiality of the subjects.

References

1. A. Dib et al., “Practical face reconstruction via differentiable ray tracing,” *Comput. Graph. Forum* **40**(2), 153–164 (2021).
2. C. Li et al., “Specular highlight removal in facial images,” in *Proc. IEEE Conf. Comput. Vis. and Pattern Recognit.*, pp. 3107–3116 (2017).
3. Z. Husain and T. S. Alster, “The role of lasers and intense pulsed light technology in dermatology,” *Clin. Cosmetic Investig. Dermatol.* **9**, 29–40 (2016).
4. E. R. Tkaczyk, “Innovations and developments in dermatologic non-invasive optical imaging and potential clinical applications,” *Acta Dermato-Venereol. Suppl* **218**, 5–13 (2017).
5. D. A. Boas et al., “Imaging the body with diffuse optical tomography,” *IEEE Signal Process. Mag.* **18**(6), 57–75 (2001).
6. A. G. Podoleanu, “Optical coherence tomography,” *J. Microsc.* **247**(3), 209–219 (2012).
7. S. Gioux, A. Mazhar, and D. J. Cuccia, “Spatial frequency domain imaging in 2019: principles, applications, and perspectives,” *J. Biomed. Opt.* **24**(7), 071613 (2019).
8. B. K. Koh, C. K. Lee, and K. Chae, “Photorejuvenation with submillisecond neodymium-doped yttrium aluminum garnet (1,064 nm) laser: a 24-week follow-up,” *Dermatol. Surg.* **36**(3), 355–362 (2010).
9. B. Hersant et al., “Assessment tools for facial rejuvenation treatment: a review,” *Aesthetic Plastic Surg.* **40**(4), 556–565 (2016).
10. H.-S. Gang, B.-S. Jeong, and B.-J. Jeong, “Real-time automatic analysis of facial skin chromophore: dermavision,” in *Proc. Opt. Soc. of Korea Conf.*, Optical Society of Korea, pp. 185–186 (2006).

11. X. Wang et al., "Comparison of two kinds of skin imaging analysis software: visia from canfield and IPP from media cybernetics," *Skin Res. Technol.* **24**(3), 379–385 (2018).
12. Y. Tani, H. Akai, and K. Akai, "New skin analyzing system-robo skin analyzer," (2004).
13. K. Kim, Y.-H. Choi, and E. Hwang, "Wrinkle feature-based skin age estimation scheme," in *IEEE Int. Conf. Multimedia and Expo*, IEEE, pp. 1222–1225 (2009).
14. Y.-H. Choi et al., "Skin feature extraction and processing model for statistical skin age estimation," *Multimedia Tools Appl.* **64**(2), 227–247 (2013).
15. J. Sun et al., "Automatic facial pore analysis system using multi-scale pore detection," *Skin Res. Technol.* **23**(3), 354–362 (2017).
16. N. Tsumura et al., "Image-based skin color and texture analysis/synthesis by extracting hemoglobin and melanin information in the skin," in *ACM SIGGRAPH 2003 Papers*, pp. 770–779 (2003).
17. B. Jung et al., "Characterization of port wine stain skin erythema and melanin content using cross-polarized diffuse reflectance imaging," *Lasers Surg. Med.* **34**(2), 174–181 (2004).
18. S. Alotaibi and W. A. P. Smith, "BiofaceNet: deep biophysical face image interpretation," in *Proc. Br. Mach. Vis. Conf. (BMVC)* (2019).
19. I. Nishidate, Y. Aizu, and H. Mishina, "Estimation of melanin and hemoglobin in skin tissue using multiple regression analysis aided by monte carlo simulation," *J. Biomed. Opt.* **9**(4), 700–710 (2004).
20. H. Jonasson et al., "In vivo characterization of light scattering properties of human skin in the 475-to 850-nm wavelength range in a Swedish cohort," *J. Biomed. Opt.* **23**(12), 121608 (2018).
21. J. Dawson et al., "A theoretical and experimental study of light absorption and scattering by in vivo skin," *Phys. Med. Biol.* **25**(4), 695 (1980).
22. E. A. Thibodeau and J. A. D'Ambrosio, "Measurement of lip and skin pigmentation using reflectance spectrophotometry," *Eur. J. Oral Sci.* **105**(4), 373–375 (1997).
23. Y. Masuda et al., "An innovative method to measure skin pigmentation," *Skin Res. Technol.* **15**(2), 224–229 (2009).
24. G. N. Stamatas and N. Kollias, "Blood stasis contributions to the perception of skin pigmentation," *J. Biomed. Opt.* **9**(2), 315–322 (2004).
25. M. Afifi et al., "CIE XYZ Net: unprocessing images for low-level computer vision tasks," *IEEE Trans. Pattern Anal. Mach. Intell.* **44**(9), 4688–4700 (2021).
26. S.-H. Tseng and M.-F. Hou, "Analysis of a diffusion-model-based approach for efficient quantification of superficial tissue properties," *Opt. Lett.* **35**(22), 3739–3741 (2010).
27. L. Wang, S. L. Jacques, and L. Zheng, "MCML—Monte Carlo modeling of light transport in multi-layered tissues," *Comput. Methods Programs Biomed.* **47**(2), 131–146 (1995).
28. G. Jung and J. G. Kim, "An approach for correcting optical paths of different wavelength lasers in diffusive medium based on Monte Carlo simulation," *Opt. Laser Technol.* **120**, 105712 (2019).
29. Z. Ma et al., "An inverse Monte-Carlo method for determining tissue optical properties," *Proc. SPIE* **6434**, 382–390 (2007).
30. I. Fredriksson, M. Larsson, and T. Strömberg, "Inverse Monte Carlo method in a multilayered tissue model for diffuse reflectance spectroscopy," *J. Biomed. Opt.* **17**(4), 047004 (2012).
31. M. Hirose et al., "Principal component analysis for surface reflection components and structure in facial images and synthesis of facial images for various ages," *Opt. Rev.* **24**(4), 517–528 (2017).
32. N. Tsumura, H. Haneishi, and Y. Miyake, "Independent component analysis of spectral absorbance image in human skin," *Opt. Rev.* **7**(6), 479–482 (2000).
33. Z. Liu and J. Zerubia, "Skin image illumination modeling and chromophore identification for melanoma diagnosis," *Phys. Med. Biol.* **60**(9), 3415 (2015).
34. S. J. Preece and E. Claridge, "Spectral filter optimization for the recovery of parameters which describe human skin," *IEEE Trans. Pattern Anal. Mach. Intell.* **26**(7), 913–922 (2004).

35. K. Nielsen et al., "Retrieval of the physiological state of human skin from UV–VIS reflectance spectra—a feasibility study," *J. Photochem. Photobiol. B: Biol.* **93**(1), 23–31 (2008).
36. S. L. Jacques, "Optical properties of biological tissues: a review," *Phys. Med. Biol.* **58**(11), R37 (2013).
37. J. Jiang et al., "What is the space of spectral sensitivity functions for digital color cameras?" in *IEEE Workshop on Appl. of Comput. Vis. (WACV)*, IEEE, pp. 168–179 (2013).
38. T. Igarashi et al., "The appearance of human skin: a survey," *Found. Trends Comput. Graph. Vision* **3**(1), 1–95 (2007).
39. M. Doi and S. Tominaga, "Spectral estimation of human skin color using the Kubelka-Munk theory," *Proc. SPIE* **5008**, 221–228 (2003).
40. L. Annala and I. Pölonen, "Kubelka–Munk model and stochastic model comparison in skin physical parameter retrieval," in *Computational Sciences and Artificial Intelligence in Industry: New Digital Technologies for Solving Future Societal and Economical Challenges*, T. Tuovinen, J. Periaux, and P. Neittaanmäki, eds., pp. 137–151, Springer, Cham (2022).
41. L. Kobayashi Frisk, "Diffuse reflectance spectroscopy: using a Monte Carlo method to determine chromophore compositions of tissue," (2016).
42. J. H. Lam, K. J. Tu, and S. Kim, "Narrowband diffuse reflectance spectroscopy in the 900–1000 nm wavelength region to quantify water and lipid content of turbid media," *Biomed. Opt. Express* **12**(6), 3091–3102 (2021).
43. T. M. Bydlon et al., "Chromophore based analyses of steady-state diffuse reflectance spectroscopy: current status and perspectives for clinical adoption," *J. Biophotonics* **8**(1–2), 9–24 (2015).
44. A. Krishnaswamy and G. V. Baranoski, "A biophysically-based spectral model of light interaction with human skin," *Comput. Graph. Forum* **23**(3), 331–340 (2004).
45. M. Ansari and R. Massudi, "Study of light propagation in Asian and Caucasian skins by means of the boundary element method," *Opt. Lasers Eng.* **47**(9), 965–970 (2009).
46. S. L. Jacques, R. D. Glickman, and J. A. Schwartz, "Internal absorption coefficient and threshold for pulsed laser disruption of melanosomes isolated from retinal pigment epithelium," *Proc. SPIE* **2681**, 468–477 (1996).
47. S. Jacques, "Skin optics," *Oregon Medical Laser Center News* (January 1998).
48. N. Ohta, *The Basis of Color Reproduction Engineering*, Corona-sha Co, Japan (1997).
49. V. Cheung et al., "A comparative study of the characterisation of colour cameras by means of neural networks and polynomial transforms," *Coloration Technol.* **120**(1), 19–25 (2004).
50. V. Starovoytov, E. Eldarova, and K. T. Iskakov, "Comparative analysis of the SSIM index and the Pearson coefficient as a criterion for image similarity," *Eurasian J. Math. Comput. Appl.* **8**(1), 76–90 (2020).
51. T. C. George et al., "Quantitative measurement of nuclear translocation events using similarity analysis of multispectral cellular images obtained in flow," *J. Immunol. Methods* **311**(1-2), 117–129 (2006).
52. R. Demirli et al., "RBX technology overview," Canfield Systems White Paper (2007).
53. Y. Pan et al., "Effectiveness of VISIA system in evaluating the severity of rosacea," *Skin Res. Technol.* **28**(5), 740–748 (2022).
54. C.-C. Lee et al., "Adaptive lossless steganographic scheme with centralized difference expansion," *Pattern Recognit.* **41**(6), 2097–2106 (2008).
55. N. Sun et al., "Novel neural network model for predicting susceptibility of facial post-inflammatory hyperpigmentation," *Med. Eng. Phys.* **110**, 103884 (2022).

Geunho Jung received his BS degree in biomedical engineering from Yonsei University in 2014 and his MS and PhD degrees in biomedical science and engineering from Gwangju Institute of Science and Technology in 2016 and 2020, respectively. He worked at Korea Institute of Lighting and ICT from 2020 to 2022. Since 2022, he has been working as a senior research

engineer at the AI R&D center of Lulu-lab Inc. His research interests include skin analysis using deep learning and diffuse optics.

Semin Kim received his ME degree in computer engineering from Kyungpook National University in 2008 and his PhD in information and communication engineering from Korea Advanced Institute of Science and Technology in 2014. He worked at Samsung Electronics from 2014 to 2019 and Hyundai Mobis from 2019 to 2021. Since 2021, he has been working as a principal research engineer at Lulu-lab, Inc. His research interests include image recognitions with deep learning and implementation of image inference systems.

Jongha Lee received his BS degree in electronics from Kyungpook National University in 1999 and his MS degree in electrical engineering from Seoul National University in 2001. He worked at Samsung Advanced Institute of Technology until 2014 and Samsung Electronics as a senior engineer for medical image processing and radiography systems. Since 2021, he has been working at the AI R&D Center of Lulu-lab as Director. His research interests include machine learning and computer vision.

Sangwook Yoo received his BS degree in computer science from Sogang University in 2005 and his MS and PhD degrees in computer science from Korea Advanced Institute of Science and Technology in 2008 and 2013, respectively. He was working as a senior engineer in Health & Medical Equipment Business Division at Samsung Electronics. He cofounded Lulu-lab, Inc., and has served as CTO since 2017. His research interests include skin analysis using deep learning and optics and image analysis-based disease prediction.